Theory of scanning tunneling microscopy and spectroscopy: Resolution, image and field states, and thin oxide layers

by N. Garcia

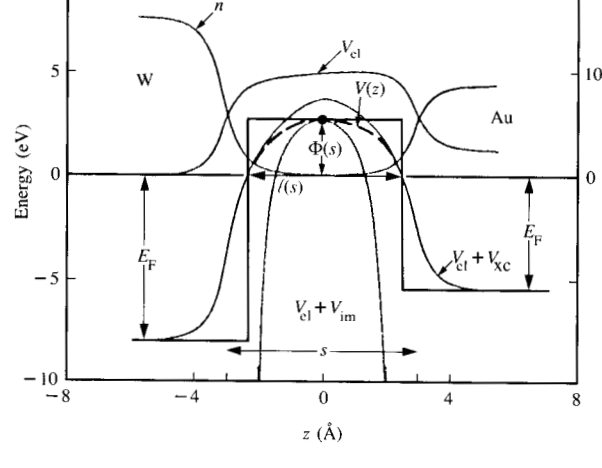
Theoretical studies on the scanning tunneling microscope and its spectroscopic version are reviewed. This research has shown that the conductance of the tunneling electrons is strongly influenced by the classical image potential. The introduction of this potential increases the conductance, although the slope of the logarithm of the conductance versus electrode separation remains practically constant. The image force also has focusing effects on the tunneling electrons and produces a minimum in the resolution for ~5 Å electrode separation. Spectroscopic levels have been

[®]Copyright 1986 by International Business Machines Corporation. Copying in printed form for private use is permitted without payment of royalty provided that (1) each reproduction is done without alteration and (2) the *Journal* reference and IBM copyright notice are included on the first page. The title and abstract, but no other portions, of this paper may be copied or distributed royalty free without further permission by computer-based and other information-service systems. Permission to *republish* any other portion of this paper must be obtained from the Editor.

calculated for the image states held by the tunneling potential. The results of this work agree very well with experimental data and indicate that the evolution of the observed tunneling spectroscopic levels with applied field is very sensitive to the image potential, and, moreover, that the whole series of image states can be obtained by extrapolation to zero applied field. Work is also presented on the theoretical aspects of tunneling spectroscopy of thin oxide layers grown on a metal substrate—NiO on Ni(100). From theory and experimental data, information can be obtained about the electronic band structure and the number of lavers of the oxide. All results of the above research are in accord with the experimental data of Binnig, Rohrer, et al. [1-3].

1. Introduction

Scanning tunneling microscopy (STM), developed by Binnig, Rohrer, Gerber, and Weibel [1] in 1982, has become a



3

10

Electron density n(z) and various potentials for a W-Au vacuum planar tunneling junction with s=6 Å. $V_{\rm el}(z)$, electrostatic potential; $V_{\rm xc}(z)$, local density exchange and correlation potential; $V_{\rm im}(z)$, image potential; V(z), tunneling potential. The dashed line is the approximate square barrier; $\Phi(s)$ is the height and I(s) is the width of the barrier.

powerful technique for the study of surface properties such as surface topography in real space and surface spectroscopy. Perhaps the most striking result in microscopy is the visualization of the Si(111) (7 \times 7) surface structure [2]. In spectroscopy, results on the characterization of the surface states of the image potential barrier as modified by an applied external field also have been presented [3]. These two results are by no means the only ones; there are examples of many other successful and remarkable experiments in all kinds of media, such as metals, superconductors, semiconductors, metallic glasses, oxides, charge density waves in lamellar compounds, and other technological and biological materials.

In the ensuing sections, this paper reviews the theoretical work on the tunneling conductivity between a tip electrode and a sample separated by a vacuum gap. The work describes the vacuum tunneling potential, in which the classical image charge force plays a major role [4, 5] in the determination of the tunneling conductivity and resolution of the tip-sample junction. This potential is also significant in the interpretation of spectroscopic levels as obtained by STM [3] and provides further information on the surface density of states and the distribution of the applied field.

Also discussed is the fact that the STM is not only sensitive to the density of states in the last layer of atoms; it can also give information on how layers grown on clean surfaces develop bulk properties. For example, one of the most studied but as yet unresolved problems is the oxidation

of metals in its initial stages, and how the first few layers achieve bulk physical properties. This is also addressed by interpreting the recent results of Binnig et al. [6] on the growth of NiO on a Ni(100) surface. Theoretical results show that the characterization of the oxide layers can be determined in a straightforward manner by examination of the experimental data.

2. Scattering theory for electron tunneling between jellium models

• Potential and image force

Potential between planar electrodes

For obtaining the tunneling conductance σ between the tip and surface, we must first define the tunneling potential for electrons tunneling in the tip-sample junction. For this we have assumed that σ for metals can be described by jellium models as shown schematically in Figure 1 for two typical metals (W, Au) of Fermi energies E_F of 8 and 5 eV, with work functions Φ of 4.5 and 5.2 eV, respectively. The potential is assumed to be a flat-bottomed well of energy $-(E_{\rm F}+\Phi)$. For small distances the surfaces of the metals are described by the local density theory for the exchange and correlation potential $V_{\rm xc}$, as derived by Lang and Kohn [7] (continuous line in Figure 1). At large distances, V_{xc} tends to the classical image potential V_{im} , as shown by theoretical considerations for the transversal time of the tunneling electrons [4]. The potential that goes from $(V_{el} + V_{xc})$ to $(V_{\rm el} + V_{\rm im})$ is indicated by the dashed line in Figure 1; $V_{\rm el}$ is the electrostatic dipole contribution to the potential. Figure 1 shows the potential calculated for two planar electrodes separated by a typical distance between jellium models of s = 6 Å and for applied voltages of ≤ 2 V. To calculate the image potential part, one must consider the existence of two image planes, located where $(V_{el} + V_{im}) \rightarrow -\infty$. The results of such calculations [5-7] indicate that the image planes are located approximately where the $(V_{el} + V_{xc})$ curve intersects the $E_{\rm F}$ line, as illustrated in Figure 1. The distance between image planes is $d = \ell(s) \simeq s - 1.5 \text{ Å [8]}$. Note that as s changes, the tunneling barrier height $\Phi(s)$ (the maximum potential energy barrier that the electrons tunnel through) changes markedly for small values of s. A reasonable approximation for $\Phi(s)$ is

$$\Phi(s) = \Phi_0 - \frac{\alpha}{d} \tag{1}$$

where Φ_0 is the average value of the work functions; d is given above, and $\alpha \simeq 9.97 \text{ eV/Å}$.

Potential for a hemispherical tip on a flat surface [5] Figure 2(a) shows the geometry of the jellium positive charge background for a hemisphere of radius $r_t = 5$ Å upon a flat surface. The sample surface is a planar electrode. The tip

and the sample surface are centrosymmetrical about the tip axis; the distance s from the apex of the tip to the sample is 6 Å and the distance between the planar parts of the tip and the sample surface is 12 Å. The system is two-dimensional; the distance in planes parallel to the sample surface at a distance z from the planar extensions of the tip, which is the distance from the intersection of the axis of the hemisphere with the plane, is given by R. The potential for small s is given by the local density theory for a spherical positive charge background of radius r, in the spherical part and as a planar electrode for the planar extensions of the tip. This potential does not include the smear-out of the charge or Smoluchowski effect [9] that tends to reduce the surface dipole and may reduce the tunneling barrier. At large distances the potential tends to the classical image potential; however, the calculation is made more complicated because of the intricate geometry required for the multiple addition of the image charges, q_i . This can be calculated by using the formula

$$V_{\rm im}(\bar{r}) = 1/2 \sum_{i} \frac{q_i}{|\bar{r} - \bar{r}_i|},$$
 (2)

where r(R, z) is the position vector, with R and z the parallel and perpendicular directions to the surface and r_i the position vectors of the multiple image charges [5].

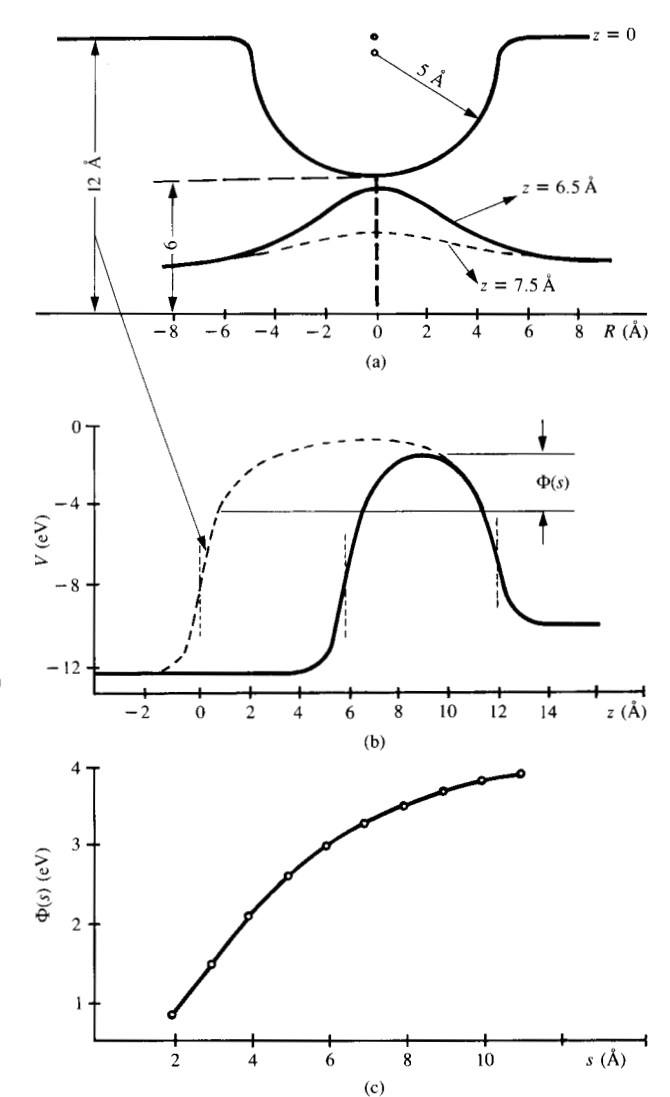
Figure 2(a) shows a plot of the potential for two values of z: The solid curve is for z=6.5 Å and the dashed one for z=7.5 Å, i.e., at 0.5 and 1.5 Å from the tip apex. This potential shows the reduction of the barrier height $\Phi(s)$ due to the geometrical configuration and the image force contribution. The potential also shows a kind of channel where the electrons may tunnel easily around the axis of the tip because of the reduction of the effective tunneling barrier. A similar result was reported in [10]. This "channel effect," as will be discussed, increases resolution and tends to reduce, $-d(\ln \sigma)/ds$, the slope of $\ln \sigma$ versus s.

Figure 2(b) shows a plot of the potential in two lines perpendicular to the flat electrode, one between flat surfaces (dashed line) and the other along the axis of the tip (continuous line) from the tip apex to the sample surface. The geometrical effect which localizes the tunneling region is again clear. There is also a non-negligible image force concentration, as can be seen in Figure 2(c), where the variation of the maximum height of the tunneling barrier $\Phi(s)$ along the tip axis [continuous line in Figure 2(b)] is plotted against s; note its variation with s and the large decrease in $\Phi(s)$ near the tip apex.

■ Lateral resolution and conductance

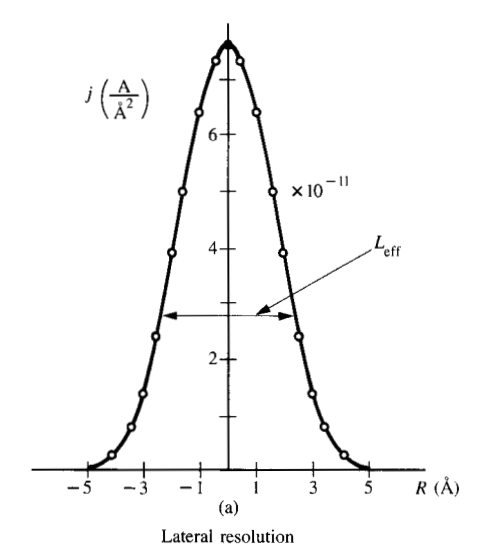
Generalities

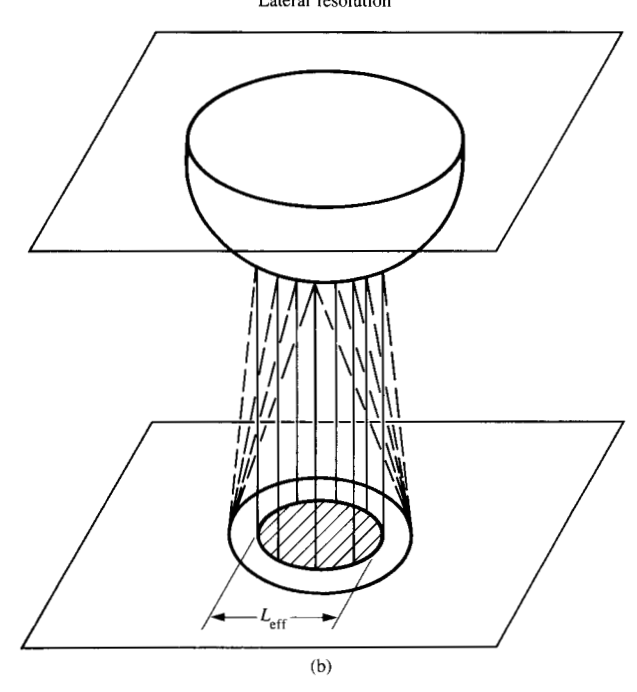
The lateral resolution $L_{\rm eff}$ is defined by the diameter of a circle which has a constant current density j equal to that obtained in the direction of the tip axis, i.e., j at R=0 [see



(a) Jellium model for a hemispherical tip on a flat surface (thick line). The other lines are plots of the tunneling potential for two values of z (z=6.5 Å, continuous line; z=7.5 Å, dashed line) as a function of R. R is the distance measured from the intersection of the axis of the hemisphere with the plane at constant z; z is measured from the planar extension of the hemispherical tip. (b) Potential lines between the flat regions of the junction (dashed line) and along the tip axis at R=0 for the geometry of Figure 1 with varying z. Φ is the barrier height for s=6 Å. (c) Variation of $\Phi(s)$ versus s, the distance from the apex of the hemisphere to the sample surface. Notice that the electron hole charge has been assumed to be spherical such that at the image plane [vertical dashed lines in (b)] $V_{\rm ex}$ and $V_{\rm im}$ are the same, namely \simeq 8 eV.

Figure 3(a)], and results in the same current, I(s), as that provided by the entire tip-sample junction. In other words, it is the effective surface area illuminated by the beam of the tunneling electrons [11]. This implies that two defects can be resolved if their separation is greater than $L_{\rm eff}$. Figure 3(b) is an illustration of the effective area and resolution. The





Figures

(a) Lateral resolution $L_{\rm eff}$ corresponding to the diameter of the effective surface area illuminated by the beam of the tunneling electrons, as shown in (b), a schematic drawing of the effective illuminated area (shaded).

formula for $L_{\rm eff}$ is

$$\pi \left(\frac{L_{\text{eff}}}{2}\right)^2 j(R=0) = I(s), \tag{3}$$

where L_{eff} , j, and the current I are functions of s. For small applied voltages V_a , I(s) is given by Ohm's law, namely

$$I(s) = V_{a}\sigma, \tag{4}$$

but for $V_a \ge 1$ V, Ohm's law is not obeyed [5].

The current I(s) can be determined by solving the following equation:

$$I = \frac{e^2}{\pi \hbar} \int_0^{V_a} dV \sum_i T[\Theta_i, (E_{Ft} - V), s],$$
 (5)

where e is the electron charge, h is Planck's constant divided by 2π , and $T(\Theta_i, s)$ is the transmission probability for the total potential of an electron with energy $(E_{\rm Ft}-V)$ and at angle Θ_i with the normal to the tip apex. The above formula is valid for large s or $T\ll 1$. If these conditions are not satisfied, the formula of Büttiker et al. [12] must be used. To calculate $T(\Theta_i, s)$, Schroedinger's equation for the potential V(R, z) must be solved.

Square potential barrier approximation

Solving Equation (5) and Schroedinger's equation for a square potential well with a constant barrier height Φ_0 , independent of z but dependent upon junction geometry, yields for the tunnel conductance [11, 13–15]

$$\sigma(d) \simeq K_0 r_1 \exp(-(\beta k d)).$$
 (6)

In Equation (6), $K_0 \simeq 1.84 \cdot 10^{-5} \text{A/(Å/eV)}$, $r_t = \text{tip radius}$, and

$$k = 1/\hbar\sqrt{2m\Phi_0},$$

where m is the electron mass. By fitting values of s, $E_{\rm F}$, and Φ into Equation (6), one obtains $\beta \simeq 2.15$, which accounts for the fact that the maximum contribution to the tunneling conductance comes from within a solid angle of 20°. (Note: σ is proportional to $r_{\rm t}$ and not to $r_{\rm t}^2$ as reported in [16].) Equation (6) fits well for $2 \le s \le 10$ Å [Recall that $d \simeq s - 1.5$ (Å)], $2 \le \Phi_0 \le 6$ eV, and $4 \le E_{\rm F} \le 11$ eV.

Values of $L_{\rm eff}$ calculated using Equations (1) and (3) are plotted in **Figure 4**, Curve A, and $L_{\rm eff}$ can be approximated [16–18] by

$$L_{\rm eff} \simeq \frac{\pi}{2} \ \sqrt{\frac{d+r_{\rm t}}{k}} \, . \label{eq:eff_loss}$$

In the above discussion, it was assumed that $\Phi(s) = \Phi_0$; however, this is not the case because of the image potential, and as shown in Equation (1), $\Phi(s) \simeq \Phi_0 - \alpha/d$. Calculations which use Equation (1) for the dependence of Φ upon s, with tip diameter $r_t = 5$ Å, $\Phi_0 = 4.8$ eV, and $E_F = 8$ eV for the sample and 5.5 eV for the tip, show that σ is 100 times larger than the σ calculated for $\Phi(s) = \text{constant} = \Phi_0 = 4.8$ eV. Moreover, the calculations also show that $-d(\ln \sigma)/ds$ (the negative slope of $\ln \sigma$ versus s) is practically constant and equal to $\beta\sqrt{\Phi_0}$. This result is in accord with the experimental observation that $-d(\ln \sigma)/ds$ remains constant even though $\Phi(s) \simeq 0$ at $s \simeq 3$ Å. For small values of s, $\Phi(s)$ is considerably reduced and is reflected in the dependence of L_{eff} upon s, as illustrated in Curve B of Figure 4, where L_{eff}

has a shallow minimum at $s \approx 5$ Å. Note that L_{eff} only varies from ~ 6 to 7 Å for $3.5 \le s \le 8$ Å, which seems to be in accord with experimental observations [13].

Three-dimensional barrier

For three-dimensional barriers, calculations of $\Phi(s)$ and σ were accomplished using other techniques [19]. The $L_{\rm eff}$ thus obtained are illustrated by Curve C in Figure 4. Examining Curve C with respect to Curve B indicates that the three-dimensional calculation yielded an increased resolution compared to the square barrier calculation. This is because of the focusing effect of the image forces, creating a channel around the tip axis where the electrons can tunnel more easily [5].

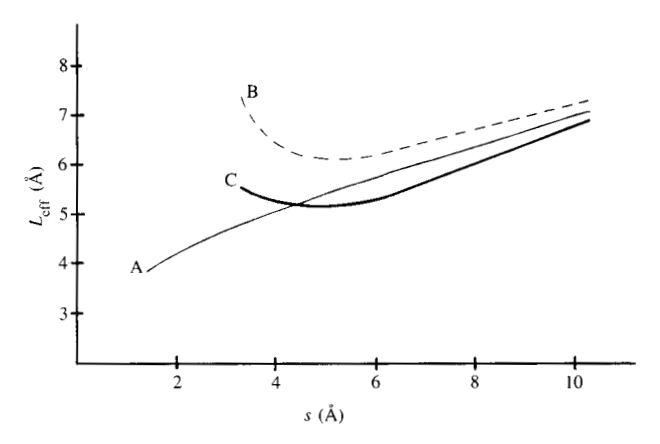
• Conductance slope; $-d(\ln \sigma)/ds$

An interesting problem in STM theory concerns the measured $-d(\ln \sigma)/ds$ [= $\sigma'(s)$]. Although constant over a large range of s, $4 \le s \le 11$ Å, in accord with theory, $\sigma'(s)$ is occasionally very small, corresponding to $\Phi \approx 0.5$ eV. This latter value of Φ is to be compared with $\Phi \approx 2-3.5$ eV for metals and for semiconductors $\Phi \approx 4-5.5$ eV. As yet there is no theoretical explanation for small $\sigma'(s)$ values. Coombs and Pethica [20] have presented evidence which proposes that small values of $\sigma'(s)$ are caused by the presence of tip irregularities in the junction.

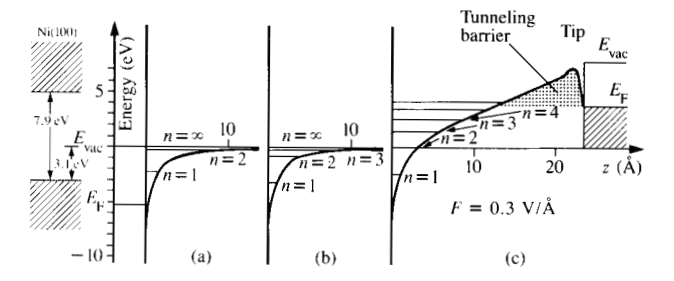
Calculations for the three-dimensional potential [5] for $V_a \le 0.1$ eV show that $\sigma'(s)$ can be reduced from the values corresponding to $\Phi = 4.8$ eV at distances s > 12 Å to values of $\sigma'(s)$ corresponding to $\Phi = 3.5$ eV for $s \simeq 5$ Å and then can be increased again if the equations of Büttiker et al. are used for calculating the conductance [12]. Small $\sigma'(s)$ values for work functions typical of metals are not obtained from this three-dimensional calculation.

3. Scanning tunneling spectroscopy for localized surface states: Image and field states

In the previous section the conductance properties of the STM were calculated using the corrugated jellium model. These calculations have pointed out that the image charge potential plays an important role in the junction conductance. The existence of image states due to the surface potential was established by inverse photoemission techniques [21, 22]. These image states introduce a large density of states at the energies where they appear in the interface and extend for distances of 2-15 Å into the interface from the last layer of atoms. They therefore should be observable in tunneling spectroscopy when V_a is such that $E_{\rm Ft}$ of the tip electrode is equal to the energy of the image states [3]. The effects of these states should be observable as oscillations in the $I-V_a$ characteristics, as predicted by Gundlach [23] for linear-barrier (field-barrier) resonances and observed experimentally in semiconductor tunneling junctions [24] and metal-metal interfaces [25], as well as in Au tips in vacuum tunneling [26].



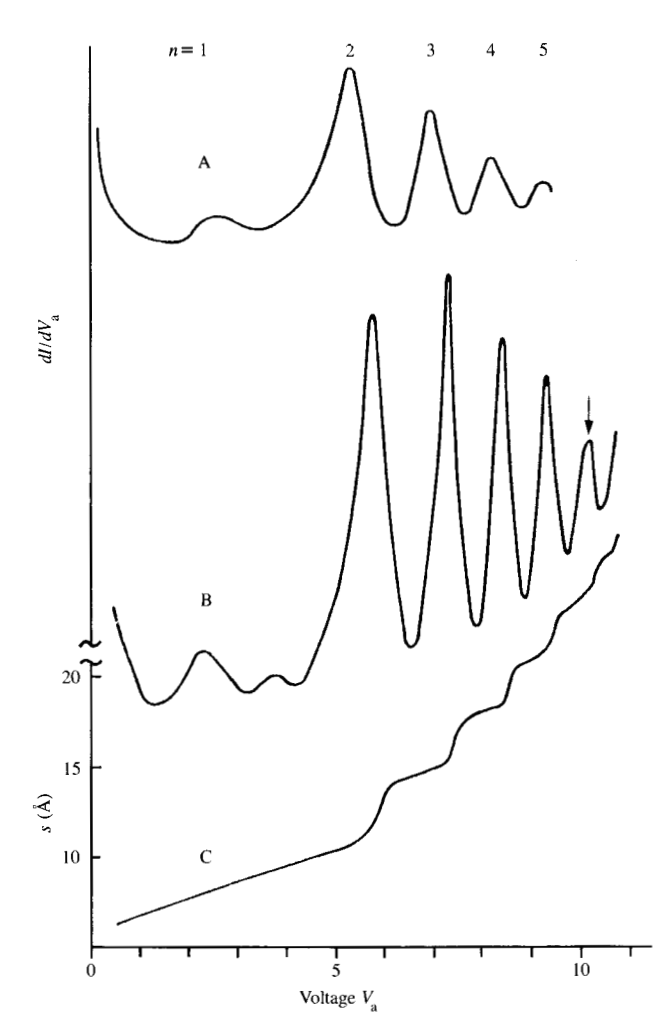
Values of $L_{\rm eff}$ versus s for the different barrier approximations. Notice in Curves B and C the minimum at $s\simeq 5$ Å in $L_{\rm eff}$ and the increase in resolution due to the image force focusing effect. Curve A represents $\Phi(s)=\Phi_0=4.8$ eV, square barrier approximation. Curve B corresponds to $\Phi(s)=\Phi_0-\alpha/d$; [Equation (1)], square barrier approximation. Curve C shows the calculated results for the three-dimensional barrier.



See a second

Energy diagram for the electrostatic potential (including image) at a metal surface. On the left, the projected bulk band structure of the Nit(100) surface is shown shaded. Note the 7.1-eV band gap straddling the vacuum level $E_{\rm vac}=0$. (a) For simplicity, only the n=1 and n=2 hydrogenic energy levels are shown. (b) The surface corrugation affects the electronic x,y movement, pulling the levels down. (c) Expansion and shift of the image-state spectrum by an applied field F. The heavy solid line is the crystal potential plus the field potential. From [3], reprinted with permission.

Figure 5 shows schematically the surface image states at a free interface and in the tunneling geometry for a Au tip and a Ni(100) surface. The characteristics of the Ni(100) surface are taken care of by introducing a gap of 7.9 eV at the surface [27–30]. The existence of this gap localizes the electron in the surface because its wave function decays exponentially into the bulk. Figure 5(a) shows schematically the free flat-surface image states $n = 1, 2, \dots, \infty$, depending upon the number of modes defining the state and ε_n energies.



Tunneling spectra dI/dV_a versus V_a , with the voltage scanned at constant tunneling current, for (Curve A) clean Ni(100) surface, (Curve B) oxygen-covered c(2 × 2) Ni(100) at low field. For Curve A, peaks are assigned to hydrogenic-like levels $n=1,2,\cdots,5$. Note the break, indicated by the arrow, in the dependence of the oscillation in Curve B at 10 V [3] (reprinted with permission). The oscillations in Curve B are proportional to the derivative of Curve C, as shown by Equation (7).

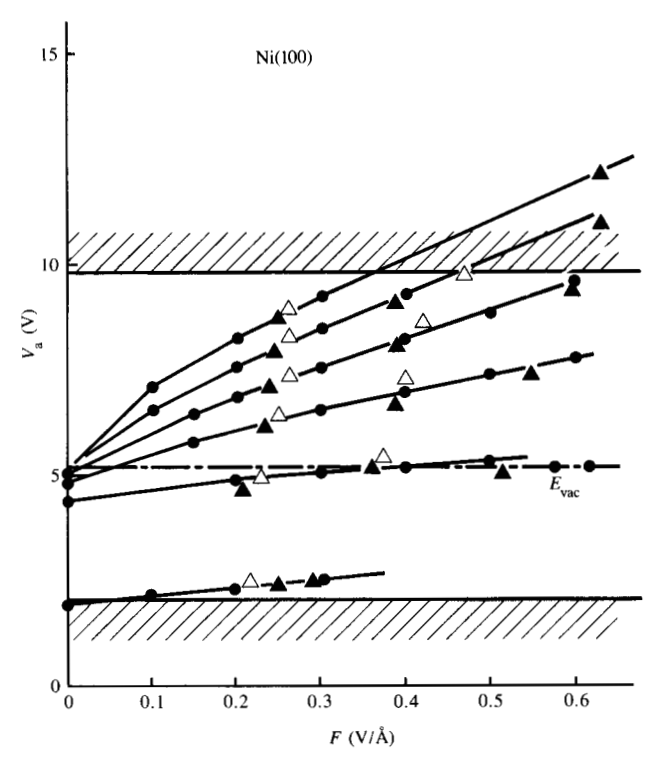
The number of states is infinite due to the long range of the image potential in analogy with hydrogenic energy levels [21, 22]. Figure 5(b) shows the same series of states, but shifted to lower energies because the real surface is corrugated by the ions [30] and having energies $E_n = \varepsilon_n + E_{\text{corr},n}$, where $E_{\text{corr},n}$ is the corrugation energy. These energy values are as observed in inverse photoemission [27–30] because they are empty states above E_F . The values of E_n are known up to n=2; however, there is no agreement as to the size of $E_{\text{corr},n}$. Figure 5(c) shows the E_n values as altered by an applied field F of 0.3 V/Å. The field is assumed constant and z-independent (because the tips in these experiments are

"blunt": ≈ 30 Å radius) in such a way that the field distribution is not complicated, and the potential is linear with distance.

Two observations should be made: 1) The infinite series of image states that accumulate in an infinite density of states near vacuum is truncated to a finite number. 2) The states increase their energy separation due to the introduction of the potential Fz (Stark effect). This has been experimentally observed [3] for several surfaces by measuring dI/dV_a . Note that in the constant-current operation mode (I constant with respect to V_a)

$$\left(\frac{\partial I}{\partial s}\right)_{V_{a}} \frac{ds}{dV_{a}} + \left(\frac{\partial I}{\partial V_{a}}\right)_{s} = 0,\tag{7}$$

and since $(\partial I/\partial s)V_a$ is a slowly varying function, $(\partial I/\partial V_a)_s \simeq -ds/dV_a$; therefore $(\partial I/\partial V_a)_s$ will be mirrored by ds/dV_a and steps in $s(V_a)$ will be transformed into peaks in ds/dV_a and $(\partial I/\partial V_a)_s$ (= dI/dV_a). The evidence for this is shown in **Figure 6**, where the undulations in s versus V_a result in the peaks in dI/dV_a (Curve A) and in ds/dV_a (Curve B) [3]. The values of V_a in dI/dV_a indicate the values of the energy states for a



propagation and

Peak positions of dI/dV_a versus V_a tunneling spectra. The symbol represents $E_n(F)$ obtained from numerical integration of the Schrodinger equation by introducing into the Hamiltonian the field potential Fz. The \triangle and \triangle symbols are for the clean Ni(100) surface. The hatched area denotes the Ni(100) projected bulk band structure. From [3], reprinted with permission.

given applied field $E_n(F)$. At the limit $F \to 0$ the image-state series E_n will be recovered. Experimentally, $E_n(F)$ versus F can be obtained; this should give useful information because the large separation in energy of the states of different n allows the improved resolution of their energies. Figure 7 shows the evolution of $E_n(F)$ for the Ni(100) surface.

A theoretical analysis [3] consistent with a unidimensional *n*-dependent Hamiltonian,

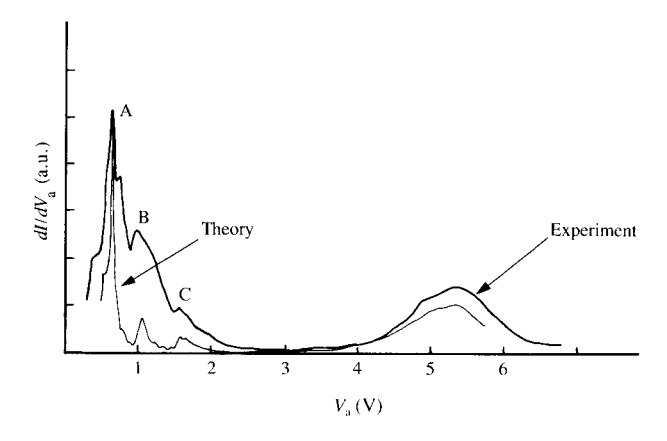
$$\mathscr{A}_n = -\left(\frac{\hbar^2}{2m}\right)\frac{d^2}{dz^2} + V_n(z) + Fz,\tag{8}$$

in which $V_n(z)$ contains the image potential as previously described for plane electrodes, plus a dipole layer region which is *n*-dependent and accounts for the corrugation potential to the surface, gives information about the image and field states. Also, the bulk potential is described by a sinusoidal potential that opens a gap of 7.9 eV as indicated above. For values of z up to 5 Å, and with the image plane at z = 0.8 Å, the value of F is much smaller than dV_n/dz , the derivative of the image potential at these distances. Therefore, at small values of z the surface potential $V_n(z)$ is stronger than the applied field potential and can be considered as a perturbation. In this Hamiltonian the only parameter is the surface dipole layer, which is adjusted so that at F = 0 the correct energy $E_n(F = 0)$ is obtained. By varying F the model gives the evolution of the (image + field) states.

Table 1 gives the energy values for Ni(100) that fit the data of Figure 7. The values of E_n are in agreement with photoemission data of Johnson and Smith [27], and it should be noted that this does not depend upon the validity of $E_{corr,n}$ [i.e., the only energy that enters our calculation is E_n , and there is only one set of E_n that fits all the $E_n(F)$ as shown in Figure 7]. Analysis of the calculated wave functions shows that $E_n(F)$ is extremely sensitive to $E_n(F=0)$. The values of $E_n(F)$, n < 2 are dominated by the image potential; Fz is only a perturbation. $E_n(F)$, n > 4 are dominated by the Fz potential; they are called field states, and n = 3 is an intermediate situation between image and field states.

The presence of image states does not require the existence of a gap such as exists in Ni(100). If there is no gap, the surface image states transform into surface image resonances as in Figure 7, $V_a < \sim 2$ eV and $V_a > \sim 10$ eV, and in [26]. Recently Becker and Golovchenko have also observed these resonances, but have not identified them in terms of image stages [31].

We have found that even if the image state is in a crystal gap it can carry current because of its width and finite lifetime, as calculated by Echenique and Pendry [32] and discussed by Flores [33]. This is in contrast to the recent results of Becker and Golovchenko [31], who claim that surface image states cannot contribute to the tunneling current because of the two-dimensional character of these



Experimental and theoretical results of STM spectroscopy on thin oxide layers. The three peaks A, B, and C indicate the oxide layers. The curve labeled Theory is calculated by using the model shown in Figure 9.

Table 1 Zero-field values of binding energies E_n , reference binding energies e_n , and corrugation energies $E_{\text{corr},n}$.

n	Ni(100)		
	E_n	ε_n	E _{corr,n}
1	-3.25	-2.40	-0.85
2	-0.85	-0.33	-0.52
3	-0.365	-0.125	-0.24
4	-0.18	-0.065	-0.12
5	-0.10	-0.040	-0.06

states. Kaiser and Jaklevic have also presented results on the spectroscopy of surface states [34].

4. Tunneling spectroscopy on thin oxide layers [35]

The characteristics of dI/dV_a versus V_a can be obtained not only for clean metal surfaces, but also for surfaces with a monolayer of adsorbate, as shown in Figure 6. Such experiments were done by Jaklevic and Lambe [36] for thin metal films with oxide tunneling junctions. Recently Binnig et al. [6] have performed spectroscopic experiments on NiO grown on Ni(100) by letting O₂ into the vacuum chamber after the experiment on Ni(100), the results of which are shown in Figure 6. They observed, by scanning and performing spectroscopy at certain areas of the surface, very large peaks in dI/dV_a [6, 37]. Figure 8 shows the experimental results in the region where the oxide layers were growing; such peaks were not present for the clean metal surface or for the $c(2 \times 2)$ structure of oxygen. Binnig et al. [6] ascribe this strong peak to the empty d band in NiO, as shown by local density band structure calculations

Electron tunneling through thin metal oxides

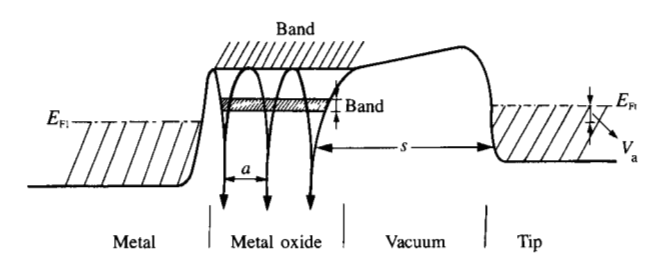


Figure 9

Model for a vacuum tunneling gap s and three oxide layers. The oxide potential is described by δ functions and the metals by jelliums. Notice the decrease of the applied potential in the vacuum gap due to the large oxide dielectric constant.

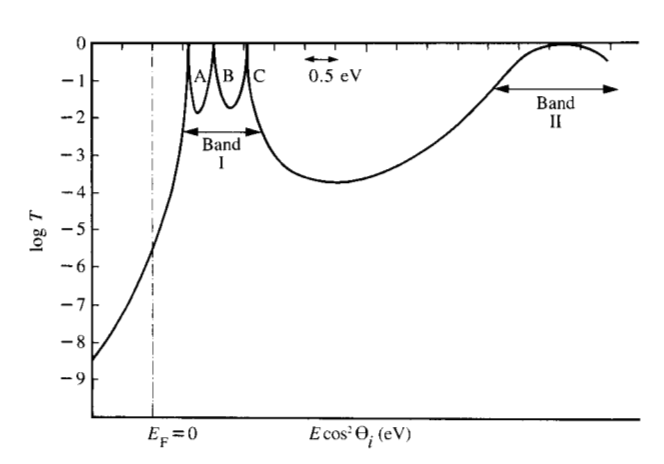


Figure 10

Transmittivity T for the tunneling electrons through three oxide layers, for s=0 (no vacuum gap—see Figure 8) versus $E\cos^2\theta_i$ (electron energy in a direction perpendicular to the junction). The A, B, and C peaks correspond very well with the energies of the A, B, and C experimental peaks in Figure 9.

by Terakura et al. [38], and the peak at $V_{\rm a} \simeq 5.5$ V was attributed to the s band of Ni in NiO [38, 39]. Identification of the observed data as tunneling phenomena via tunneling theoretical calculations was not performed. A tunneling interpretation is very appealing because if such bands exist, when an electron tunnels with its energy in the range of the oxide band it ceases to be a tunneling electron; i.e., it is described not by an evanescent wave but by a propagating one in the oxide region. Therefore, if there are several layers of oxide, the conductance at the band edge energy will have a large increase, as suggested by the data [6].

To calculate tunneling conductance, the model shown in **Figure 9** is proposed for the metal-oxide-vacuum-metal junction [6]. The oxide is described by a one-dimensional set of potential barriers (in our case δ functions):

$$V_{\text{oxide}} = V_0 - \alpha \sum_{j=1}^{j=N} \delta(ja - z), \tag{9}$$

where V_0 is the background potential, α is the δ function strength, N is the number of layers, and a is the interspacing of the oxide layers. This model has been used to calculate conductivity properties through oxides [40] and also by Tsu and Esaki [41] to calculate transport properties by multibarrier tunneling in superlattices. Its one-dimensionality is not a problem because we are concerned with the conductivity in the z-direction, and this implies that the multiband scattering in the (x, y) direction should not be important. The tip is "blunt," $r_t \approx 30$ Å, and for the electron of ≈ 5 Å wavelength this is practically a planar junction. The calculations were performed with these "large" tips in order to avoid complicated field distributions and to have "practically" planar electrodes.

The model assumes a = 3.5 Å for the interplanar spacing in the close-packed crystallographic direction in NiO. A constant value for $\alpha = 5$ eV-Å was chosen so as to ensure that as $N \to \infty$ the first band would have the theoretical d bandwidth ~ 1.2 eV [38, 39]. The parameter V_0 is fixed to obtain a large peak in the value of the transmittivity in agreement with the experiment at $V_a \simeq 0.6 \text{ V}$ ($V_0 = 2.6 \text{ eV}$ above the Ni Fermi level). The model also accounts for the image potential at the tip interface as well as for the external potential that is linear and decreases largely in the vacuum gap region because of the large dielectric constant of the oxide. This is schematically indicated in Figure 9. The three experimental peaks are indicated in Figure 8 by points A, B, and C; note that their energy positions correspond very well to the three theoretical peaks. The large experimental peak A is located just 0.05 eV to the left of peak A. The experimental peak A appears as a consequence of the rapid increase in transmittivity (conductivity) of the oxide layers. **Figure 10** shows the calculated values of $T(\Theta_i)$ for the three oxide layers and s = 0 as indicated in Figure 9. The first band (I) appears at $V_a \simeq 0.6$ V because of the assumed value for V_0 . Notice the appearance of a second band (II) in agreement with [40, 41] a higher oxide conduction band at $V_{\rm a} \simeq 7 \text{ eV}$ above $E_{\rm F}$. This second band corresponds to the experimental peak located at 5.5 eV above E_F , not only in position but also in shape, and the peak is broad because the conductivity increases at a lower rate than does the conductivity for the peaks in band I.

The results of a more extensive calculation [6] for I(s) and dI/dV_a are indicated by the curve labeled "Theory" in Figure 8. In this calculation the integration in Equation (5) was performed over all values of Θ_i for each V_a for the condition $I = \text{constant} \simeq 1 \text{ nA}$. The calculation proceeds by finding the value of s (=5-6 Å) which will provide a current density of about 10^{-11} to 10^{-12} A/Ų and in turn gives an I(s) of 10^{-8} to 10^{-9} A for an area of ~500 Ų (recall that $r_t \simeq 30$ Å). Finally, dI/dV_a is obtained from Equation (7). The "Theory" curve in Figure 8 shows the remarkable agreement obtained

with these calculations and the experimental data, and one can conclude that these observations can indeed be attributed to the tunneling of electrons in NiO layers.

The results of these calculations show that

- 1. The number of oxide layers is three because of the three experimental peaks; if we introduce N layers, N peaks are observed in the same energy range, ~1 eV energy bandwidth.
- 2. There is clearly a second oxide band.
- 3. These results are in very good agreement with the band structure calculations of Terakura et al. [38] and Kubler and Williams [39].

5. Conclusions

We have presented theoretical aspects of our STM research. Topographic microscopy and spectroscopic results on clean adsorbed monolayers and thin oxide layers have been discussed. From the results the following conclusions are inferred:

- 1. In the determination of the conductance or current intensity in STM, the tunneling potential barrier is basically dominated by the classical contribution of the image potential [5, 13], in agreement with the theoretical studies for the tunneling electron transversal time [4]. The image contribution reduces the height of the tunneling barrier $\Phi(s)$ from the work function Φ_0 at $s \to \infty$, and to zero when the electrode separation is $s \simeq 3$ Å. The $\sigma'(s)$ remains practically constant and in the range corresponding to a barrier height of $\Phi \simeq 1.5$ eV. However, the values of σ are reduced by a factor of \sim 100 compared to the value obtained for a constant barrier, $\Phi_0 \simeq 5$ eV. Finally, the influence of the image force has a focusing effect on the resolution $L_{\rm eff}$, which is a minimum at $s \simeq 5$ -6 Å.
- 2. It has been shown that image force is important in determining the empty electronic states, as observed experimentally [3]. These surface image states as corrected by the applied field have a one-dimensional character up to distances of ~2 Å from the last layers of atoms and have important energy contributions from the modulation of the potential in the region core. The STM in its spectroscopic version is a powerful technique for detecting localized surface states and is able to unravel the series of image states because of the shift produced by the applied external field between surface and tip. These states are pure surface states if the material has a gap at their binding energies and a resonance otherwise [21, 26]. Even if they are pure surface states, they can carry current because their lifetime is shorter than the tunneling time for the electrons [32, 33].
- 3. From our analysis in tunneling through thin oxide layers we believe that the spectroscopic version of the STM can

give information about the electronic and geometrical properties of thin layers grown or deposited on a substrate. We have used our calculations to understand the growth and experimental data [6] of NiO layers on Ni(100). The calculated results show very good agreement with the data and are able to resolve the number of layers grown (three in this case) as well as the density of states or conduction bands of the oxide film. The calculations are in agreement with local density band structure calculations [38, 39]. These results open new perspectives in the characterization of the growth and nucleation of thin films on solid substrates.

Acknowledgments

It is a pleasure to acknowledge discussions and work done with my colleagues G. Binnig, H. Rohrer, and A. R. Williams from IBM, as well as J. M. Soler and my students R. Garcia and J. J. Saenz. This work has been supported by the Comision Asesora de Investigacion Científica y Técnica through Contract No. 1426-82 and by the Centro Científico (UAM-IBM). I also thank the IBM Europe Scientific Institute for inviting me to the STM Workshop held at Lech, Austria, July 1985.

References and notes

- G. Binnig, H. Rohrer, Ch. Gerber, and E. Weibel, Appl. Phys. Lett. 40, 178 (1982); G. Binnig and H. Rohrer, Helv. Phys. Acta 55, 726 (1983) and references therein.
- G. Binnig, H. Rohrer, Ch. Gerber, and E. Weibel, *Phys. Rev. Lett.* 50, 120 (1983).
- G. Binnig, K. H. Frank, H. Fuchs, N. Garcia, B. Reihl, H. Rohrer, F. Salvan, and A. R. Williams, *Phys. Rev. Lett.* 55, 991 (1985).
- M. Büttiker and R. Landauer, Phys. Rev. Lett. 49, 1739 (1982); and IBM J. Res. Develop. 30, No. 5, 451-454 (1986, this issue).
- R. Garcia, J. J. Saenz, J. M. Soler, and N. Garcia, J. Phys. C 19, L131 (1986).
- R. Garcia, J. J. Saenz, and N. Garcia, *Phys. Rev. B* 33, 4439 (1986).
- N. D. Lang and W. Kohn, Phys. Rev. B 1, 4555 (1970); N. D. Lang, Solid State Phys. 28, 225 (1973).
- 8. Notice that s is the distance between jellium edges. The distance that separates the last layer of nuclei for a perfect geometry (i.e., not relaxed or reconstructed surface) is $s + d_1/2 + d_2/2$, where d_1 and d_2 are the interplanar spacing metal surfaces forming the electrodes.
- 9. R. Smoluchowski, Phys. Rev. 60, 661 (1941).
- A. A. Lucas, J. P. Vigneron, J. Bono, P. H. Cutler, T. E. Feuchtwang, R. H. Good, and Z. Huang, J. de Physique C9, 125 (1984).
- N. Garcia, C. Ocal, and F. Flores, Phys. Rev. Lett. 50, 2002 (1983).
- M. Büttiker, Y. Imry, R. Landauer, and S. Pinhas, *Phys. Rev. B* 31, 6207 (1985).
- G. Binnig, N. Garcia, H. Rohrer, J. M. Soler, and F. Flores, *Phys. Rev. B* 30, 4816 (1984).
- E. Stoll, A. Baratoff, A. Selloni, and P. Carnevali, J. Phys. C 17, 3073 (1984).
- 15. N. Garcia and F. Flores, Physica 127B, 137 (1984).
- J. Tersoff and D. R. Hamann, Phys. Rev. Lett. 50, 1998 (1983);
 Phys. Rev. B 31, 805 (1985).
- 17. E. Stoll, Surf. Sci. 143, L4111 (1984).
- 18. A. Baratoff, Physica 127B, 143 (1984).
- 19. R. G. Gordon, J. Chem. Phys. 51, 14 (1969).

- J. H. Coombs and J. B. Pethica, IBM J. Res. Develop. 30, No. 5, 455–459 (1986, this issue).
- 21. N. Garcia and J. Solana, Surf. Sci. 36, 262 (1973).
- 22. E. G. McRae, Rev. Mod. Phys. 51, 541 (1979).
- 23. K. H. Gundlach, Solid State Electron. 9, 949 (1966).
- 24. J. Maserjian and N. Zamani, J. Appl. Phys. 53, 559 (1982).
- B. T. Jonker, N. C. Bartelt, and R. L. Park, Surf. Sci. 127, 183 (1983).
- 26. G. Binnig and H. Rohrer, Helv. Phys. Acta 55, 726 (1982).
- 27. P. D. Johnson and N. V. Smith, Phys. Rev. B 27, 2527 (1983).
- V. Dose, W. Altmann, A. Goldmann, U. Kolac, and J. Rogozik, *Phys. Rev. Lett.* 52, 1919 (1984).
- 29. D. Straub and F. J. Himpsel, Phys. Rev. Lett. 52, 1922 (1984).
- N. Garcia, B. Reihl, K. H. Frank, and A. R. Williams, *Phys. Rev. Lett.* 54, 591 (1984).
- 31. R. S. Becker, J. A. Golovchenko, and B. Swartzentruber, *Phys. Rev. Lett.* 55, 987 (1985).
- 32. P. M. Echenique and J. R. Pendry, J. Phys. C 11, 2065 (1978).
- 33. F. Flores, Autonomous University of Madrid, Spain, private communication.
- 34. W. J. Kaiser and R. C. Jaklevic, AT&T Laboratories, Murray Hill, NJ, private communication.
- Section 4 was written in collaboration with R. Garcia and J. J. Saenz.
- 36. R. C. Jaklevic and J. Lambe, Phys. Rev. B 12, 4146 (1975).
- 37. G. Binnig, IBM Research Division, Zurich, Switzerland, private communication. The peak observed on NiO layers, for $V_a \approx 0.6$ V, is at least ten times larger than those described in Ref. [3]. See Figure 6 of this paper.
- K. Terakura, A. R. Williams, T. Oguchi, and J. Kubler, *Phys. Rev. Lett.* 52, 1830 (1984); *Phys. Rev. B* 30, 4734 (1984).
- J. Kubler and A. R. Williams, J. Magn. & Magn. Mater. 54-57, 603-606 (1986).
- P. Schnupp, *Phys. Status Solidi* 21, 567 (1967); E. Stoll and T. Schneider, *Solid State Commun.* 11, 1327 (1972).
- 41. T. Tsu and L. Esaki, Appl. Phys. Lett. 22, 562 (1973).

Received August 6, 1985; accepted for publication May 24, 1986

N. Garcia Autonomous University of Madrid, Department of Fundamental Physics, Cantoblanco, 28049 Madrid, Spain. Professor Garcia graduated from the Universidad Complutense de Madrid with a degree in physics in 1970. He received a Ph.D. degree from the Autonomous University of Madrid in 1976, and since 1983 has held a Chair in the Department of Fundamental Physics at that school. Professor Garcia has been a visiting professor at several universities and research centers in the United States and Europe. His research interests include He surface scattering, light scattering, oxide growth, and quantum interference effects. He has recently been engaged in the application of scanning tunneling microscopy to biology, metrology, and industrial problems.